

Article

Enhancing Thermal Performance, Exergy and Thermodynamics Efficiency of Premixed Methane/Air Micro-Planar Combustor in Micro-Thermophotovoltaic Systems

Jinshen Tong * and Tao Cai

Department of Mechanical Engineering, University of Canterbury, Christchurch 8041, New Zealand

* Correspondence: jto66@uclive.ac.nz

Abstract: The present work numerically investigates the effect of a cavity implemented in a premixed methane/air micro-combustor on enhancing its thermal performances and thermodynamic efficiencies for micro-thermophotovoltaic applications. The 3D time-domain numerical model is first validated by comparing its predictions with the experimental data available in the literature. Then it is applied to examine the effects of the cavity dimensionless axial location (x_c/L), cavity volume (V_c), the equivalence ratio ϕ and hydrogen blended ratio (α) on the temperature uniformity and enhancement of the combustor outer wall and exergy efficiency. It is found that implementing a cavity in the combustion chamber increases the outer wall mean temperature (OWMT) and the exergy efficiency up to approximately 65 K and 10%, respectively. The optimal cavity dimensionless axial location (x_c/L) is set to 1/9, and the height (H_{c_dims}) is 1/5, respectively. However, the cavity length L_c and angle θ_c are found to play negligible roles on improving thermal performance. Additionally, increasing the inlet velocity leads to a higher OWMT but a low exergy efficiency, regardless of the equivalence ratio. In general, this work confirms the feasibility of applying a cavity structure to enhance energy efficiency for micro-power generation systems.



Citation: Tong, J.; Cai, T. Enhancing Thermal Performance, Exergy and Thermodynamics Efficiency of Premixed Methane/Air Micro-Planar Combustor in Micro-Thermophotovoltaic Systems. *Energies* **2023**, *16*, 118. <https://doi.org/10.3390/en16010118>

Academic Editors: Antonio Ficarella, Maria Grazia De Giorgi and Donato Fontanarosa

Received: 22 November 2022

Revised: 13 December 2022

Accepted: 14 December 2022

Published: 22 December 2022



Copyright: © 2022 by the authors. Licensee MDPI, Basel, Switzerland. This article is an open access article distributed under the terms and conditions of the Creative Commons Attribution (CC BY) license (<https://creativecommons.org/licenses/by/4.0/>).

Keywords: thermodynamics; exergy; heat transfer; methane; thermal performance; micro-combustion

1. Introduction

The Micro-Thermophotovoltaic (MTPV) System [1,2] is a typical combustion-based power generation system, fueled by hydrogen or hydrocarbon, which has the advantages of noiseless operation, fuel versatility and portability compared to micro-gas turbine engines [3,4] and micro-fuel cells [5]. Even though it has so many outstanding advantages, the system thermodynamic and energy conversion efficiency [6] of MTPV still needs to be further improved. Such a system requires a compact, long operational lifetime and instant rechargeability [7,8].

The MTPV consists of an emitter (typically a micro-combustion heat source), a filter and a thermophotovoltaic cell array. When it is in use, the chemical energy of the fuel–air mixture releases heat via combustion [9–15] in the micro-combustor, and the outer wall surface emits thermal radiation [16]. The radiated photons with energy higher than the band-gap generate electricity through imping on the PV cell, while the others are absorbed and recycled by the filter. As a result, PV cells are also more sensitive to high-energy photons instead of total radiation power since they directly contribute to the generation of electricity. Consequently, to achieve a better energy conversion performance of the MTPV system, the micro-combustor requires a higher and more uniform wall temperature [17,18].

Unlike conventional combustors [19–21], the large surface-to-volume ratio at the millimeter scale results in a significant amount of heat loss [22], which aggravates the adverse effect on total heat generation and leads to the major issue of flame-quenching [23]. Three types of improvement strategies have been investigated to emphasize improving the micro-combustion thermal performance. The first strategy is to introduce the different

fuel properties [24,25] and a catalytic [26] to address the thermal issue through accelerating the fuel conversion rate and the chemical reaction time of the combustion. Tang et al. [27] evaluated the premixed CH₄/air micro-combustion with hydrogen addition. It is found that the fuel with 10% hydrogen not only enhances the wall temperature and the flammability range but also stably anchors the flame location near the inlet. Similar findings can also be found in premixed propane/air micro-combustion in Ref. [28] which reported that 20% hydrogen addition leads to a reduction in quenching height from 2 mm to 1.5 mm. Sun et al. [29] studied the dilution effect of NH₃/O₂ premixed micro-combustion with incombustible gas, and the result indicates the thermal performance and NO emission are improved with CO₂ dilution. Similarly, blending NH₃/O₂ with H₂ or diesel can effectively reduce NO_x emissions [30,31] and avoid extremely high combustion temperatures, which could damage the wall material [32]. Moreover, Zheng et al. [33] have numerically exploited the synergy of the direct radiation effect and chemical effect of preheating upstream fluid, which is critical to the radiation reabsorption, and the maximum optimized effect was up to 15.6%. On the other hand, catalyst materials, including platinum and rhodium, can also promote energy conversion efficiency [34,35].

The second strategy is to recycle the heat of burned flue gas by altering the entry location of the fuel and oxide [36,37]. Zuo et al. [38] numerically investigated a four-channel Meso-combustor with different configurations. The result indicates the counter-flow channels have the highest mean wall temperature when the peak temperature point of adjacent channels is decentralized. Also, micro Swiss-roll combustors are another classic design that achieves enthalpy combustion through heat recuperation [39]. Non-premixed micro Swiss-roll combustors have an advantage in raising the flame surface and increasing the heat release amount [40]. Additionally, premixed micro Swiss-roll combustion has been experimentally conducted by Zhong and Wang [41]. It is found that the combustion stability [42,43] and temperature are greatly enhanced in the center region, and the center temperature can reach 1100 K with the thermal insulation of alumina powder.

The last strategy is to generate heat recirculation zones in the micro-combustor, which is a common method to promote heat transfer [44]. For instance, Yang et al. [45] experimentally reported that the heat recuperator inserts give rise to an increase in the wall temperature up to 123 K as a result of the preheating effect. Apart from that, two categories have been investigated: porous media insertion [46–48] and the structure design of micro-combustors. Concerning the former strategy, the porous media matrix increases the contact area, thus markedly boosting the heat transfer between the combustion region and the solid wall [49]. The inherent matrix properties promote the preheating effect on the unburned gas and decrease the flow velocity, which establishes a uniform flame distribution [50]. Yang et al. [51] experimentally discovers that the wall temperature is increased by 90–120 K with the insertion of SiC porous media. Additionally, Maghsoudi et al. [52] investigated the partially filled porous medium with different cross-section geometries. It is found that the optimal thermal performance is independent of the geometry at a porosity of 0.8.

Another category is aimed at changing the inner structures of the micro-combustors, which include backward-facing steps [53], bluff body [54–58], wall cavity [59,60], ribs [61–63] and their combinations [64]. In this context, many research efforts have also been devoted to improving the effective radiation energy of the micro-combustor by intensifying the internal flow field [65,66] which not only increases the turbulence intensity but also prolongs the residence time [67]. The existence of a backward-facing step changes the flame dynamics in the combustor and extends heat recirculation through the solid wall [68]. It should be noted that implementing a step in the combustor assists flow separation and vortex generation, which benefits heat transfer [69]. Additionally, the step location anchors the flame position and stability because the heat and flow recirculation form behind the step, which results in high-intense heat transfer through the combustor wall to the unburned gas [70]. Next, Peng et al. [71] numerically compared a micro-combustor with and without a front cavity. The result shows that the micro-cavity combustor has a higher outer wall temperature because of the flow hysteresis effect, and the micro-cylindrical combustor with

an arc-shaped cavity has the optimal thermal performance compared with trigonal, rectangular and isosceles. Similarly, a micro-cylindrical combustor with a cavity numerically achieves a mean outer wall temperature of 1306.88 K [72]. Moreover, Su et al. [73] have numerically studied a double-cavity micro-combustor and found that the second cavity developed a second high-temperature zone with high inlet velocity, and the radiation efficiency and uniformity have increased slightly. Furthermore, Cai et al. [74,75] numerically analyzed the effect of singular and staggered bluff bodies on the micro-combustor thermal performance. It is shown that the bluff-body contributes to generating longitudinal vortices and disrupting the formation of thermal boundary layers, hence amplifying heat and mass transfer. Additionally, the optimized dimensionless location of a singular bluff body at 2/5 and staggered bluff bodies with an appropriate height and pitch ratio increase the mean wall temperature by 57.5 K and 73 K, respectively. In addition, with the dimensionless rib located at 5/9 and a height of 0.4, the temperature can be numerically increased by 61 K, resulting in a mean wall temperature of 1284 K [76]. Lastly, several novel micro-combustors [77–82] have been developed in the past decade, aiming at improving the wall temperature and radiation energy.

Previous investigations revealed that the thermal performance of a micro-combustor can be enhanced by changing the combustor's inner structure. However, to the best knowledge of the present authors, the effects of combustor design parameters and hydrogen addition on the combustion and thermal performance in methane-fueled micro-planar combustor with a cavity are less explored. Meanwhile, how the exergy efficiency varies with such dual-fuel combustion remains unknown. These motivate the present study. In this work, a three-dimensional numerical simulation of a premixed methane/air micro-combustor with a cavity is conducted to analyze the thermal performance, heat transfer, exergy generation and hydrogen addition. In Section 2, the numerical methodologies are described in detail, including the geometry, mathematical models and model validation. In Section 3, the effects of the cavity dimensionless axial location, the cavity volume and the equivalence ratio on thermal performance are evaluated. Comparison is then made to obtain the optimum design. Further exergy and hydrogen blended effect studies are performed and described in Sections 4 and 5. The interesting findings are summarized in Section 6.

2. Numerical Methodologies

2.1. Geometric Model

The physical geometry of the micro-combustor with a cavity is shown in Figure 1. The total length, width and height of the combustor wall are set as L , W and H along the x , y and z -direction respectively, while the wall thickness is T . A cavity lies symmetrically along the x - y plane, and it has a trapezoidal shape on each side with a horizontal length (L_c), a vertical depth (H_c), a horizontal width (W_c) and two equal angles (θ_c), respectively. The distance from the inlet plane to the left-side point of the incline angle is x_c . Finally, the dimensions of the micro-combustor are summarized in Table 1.

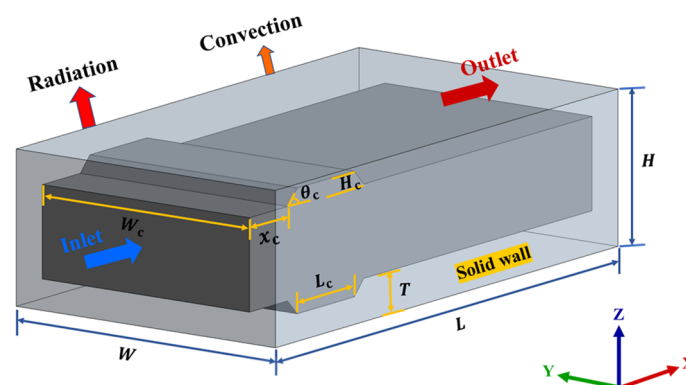


Figure 1. Schematic diagram of the premixed micro-combustor with a cavity implemented.

Table 1. Dimensions of the micro-cavity combustor.

Parameters	Values (mm)
L	18
W	10
H	5
T	1
x_c	2, 4, 6, 8
L_c	1, 3, 5
W_c	8

2.2. Mathematical Model

To simplify the numerical model of combustion, the following assumptions are made: (1) The methane/air mixture is a continuum fluid, and thus, the Navier-Stokes equation is applicable; (2) the combustion obtains a steady state at the equilibrium status; (3) the methane/air mixture is assumed ideal gas, and the flow is uniform; (4) no surface reaction and Dufour effect [83] in the combustion region; (5) no work done by the pressure, body force and viscous force; and (6) the governing equations related to the numerical model are solved using ANSYS Fluent 2020 and are summarized below.

Mass conservation

$$\nabla \cdot (\rho \vec{v}) = 0, \quad (1)$$

where ρ is the fluid density and \vec{v} is the velocity vector ($\vec{v} = (u, v, w)$) in x, y, z Cartesian coordinates.

Momentum conservation

$$\nabla \cdot (\rho \vec{v} \vec{v} - \vec{\tau}) = -\nabla p, \quad (2)$$

where p is the static pressure and $\vec{\tau}$ is the stress tensor (described below).

$$\vec{\tau} = \mu [(\nabla \vec{v} + \nabla \vec{v}^T) - \frac{2}{3} \nabla \cdot \vec{v} I], \quad (3)$$

where μ is the molecular viscosity; I is the unit tensor; and the second term on the right-hand side is the effect of volume dilation.

Energy balance equation for species

$$\nabla \cdot (\vec{v} (\rho E + p)) = \nabla \cdot \left(k_{eff} \nabla T - \sum_j h_j \vec{J}_j + (\vec{\tau} \cdot \vec{v}) \right) + S_h \quad (4)$$

where E is the total fluid energy; k_{eff} is the effective conductivity; T is the temperature; h_j is the enthalpy of species j ; \vec{J}_j is the diffusion flux of species j ; and S_h is the fluid enthalpy source term.

Species equations

$$\nabla \cdot (\rho \vec{v} Y_i + \vec{J}_i) = R_i, \quad (5)$$

where R_i is the net rate of production of species i by chemical reaction; Y_i is the local mass fraction of each species; and \vec{J}_i is the diffusion flux of species i in the mixture.

Wall energy conservation equation

$$\nabla \cdot (k_{ij} \nabla T) = 0, \quad (6)$$

where k_{ij} is the thermal conductivity of the solid wall.

The total energy loss from the combustor outer wall to the ambient environment

$$Q_{loss} = \sum_{i=1}^n h_i A_i (T_{w,i} - T_0) + \sum_{i=1}^n \varepsilon \sigma A_i (T_{w,i}^4 - T_0^4), \quad (7)$$

where h_i is the thermal convection coefficient; T_0 is the ambient temperature; ε is the emissivity of the solid wall; and σ is the Stefan-Boltzmann constant ($5.67 \times 10^{-8} \frac{W}{m^2 K^4}$).

Area-weighted-average wall temperature

$$\bar{T}_w = \frac{1}{A} \sum_{i=1}^n T_i A_i, \quad (8)$$

where A is the surface area; T_i is the temperature of grid cell i on the wall; and \bar{T}_w is the mean wall temperature.

The standard deviation of the wall temperature

$$R_{T,w} = \sqrt{\sum \left(\frac{T_i - \bar{T}_w}{\bar{T}_w} \right)^2}. \quad (9)$$

2.3. Numerical Model and Boundary Conditions

The methane/air premixed combustion characteristics of the numerical model involve the coupling of fluid dynamics, heat and mass transfer and chemical reactions; hence, the laminar model, finite-rate species transport model and energy model are applied in the simulation. A reaction mechanism with 17 volumetric species and 25 reversible reactions in this model, and a stiff chemistry solver is selected to solve the intra-phase and interphase chemical reactions. The reaction mechanism employed in this study was originally developed by Smooke and Giovangigli [84]. This mechanism was widely applied in numerical simulations [85]. It also shows a strong applicability in predicting the combustion process in the current study, as described in Section 2.5. The density and mass diffusivity of the gas mixture are calculated by using incompressible-ideal-gas and kinetic theory, and specific heat, thermal conductivity and viscosity are calculated using the mixing law. The stainless steel 316 is selected as the solid wall with density, specific heat and thermal convection coefficient of 8000 kg/m^3 , $500 \text{ J/(kg} \cdot \text{K)}$ and $18 \text{ W/(m} \cdot \text{K)}$, respectively. The boundary conditions of the numerical model are listed in Table 2. The governing equations are discretized using the second-order upwind scheme, while the pressure-velocity coupling is solved using the SIMPLE algorithm. The under-relaxation factors of density, body forces, species and energy are set to 0.9. All residual absolute criteria of the equations are set to be less than 1×10^{-6} .

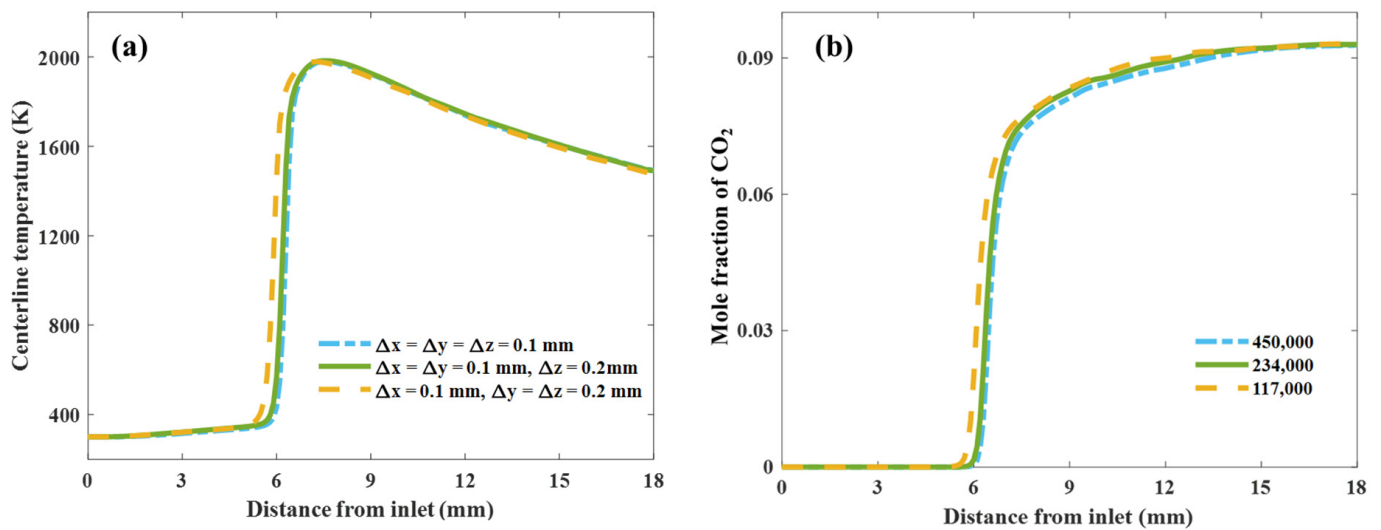
2.4. Grid Independence Study

Because of the symmetry of the model along the $y = 0$ plane, one-half of the geometry is employed as the computational domain to save the calculation time. The computational domain ($L, W, \frac{1}{2}H$) of the 3-dimensional micro-combustor without cavity uses a structured quad mesh of ANSYS Meshing 2020 for grid generation. A grid independence study is conducted where the equivalence ratio and velocity are set to 1.0 and 0.6 m/s, respectively. Three different mesh densities of the combustor computational domain with 450,000 cells (0.1, 0.1, 0.1), 234,000 cells (0.1, 0.1, 0.2) and 117,000 cells (0.1, 0.2, 0.2) are applied in the simulation. The centerline temperature and CO_2 mole fraction profiles of the $y = 0$ plane are depicted in Figure 2.

It is seen that both the calculated centerline temperature and CO_2 mole fraction are highly overlapped with the medium mesh (234,000 cells) and with the fine mesh (450,000 cells). However, a significant difference occurs between the coarse mesh (117,000 cells) and the other two mesh densities. Therefore, the medium mesh is selected in this study to obtain a solution for better accuracy and the least computational complexity.

Table 2. The boundary conditions of the numerical model.

Boundary Conditions	Parameters	Values
Inlet (velocity-inlet)	Velocity magnitude (m/s)	0.4, 0.6, 0.8, 1.0
	Gauge pressure (Pa)	0
	The equivalence ratio ϕ	0.9, 1.0, 1.1
	Atmospheric temperature (K)	300
	Species mole fractions	Based on the equivalence ratio
Outlet (pressure-outlet)	Gauge pressure (Pa)	
Inner wall	Wall motion	Stationary wall
	Shear condition	No slip
	Thermal conditions	Coupled
	Material	Stainless steel 316
	Species	Zero diffusive flux
Outer wall	Thermal conditions	Mixed
	Material	Stainless steel 316
	Heat transfer coefficient (W/(m ² ·K))	15
	Free stream temperature (K)	300
	External emissivity	0.65
	External radiation temperature (K)	300

**Figure 2.** Profiles of (a) Centerline temperature and (b) CO₂ mole fraction at $y = 0$ planes by applying three mesh densities.

2.5. Model Verification

To verify the accuracy of the numerical model, the computational results have been compared with the experimental measurement in the previous work [29]. The centerline temperature profile along the flow direction at two different inlet velocity conditions is illustrated in Figure 3. The maximum deviation of temperature is 6.4% and 2.8% at the inlet velocities of 0.4 m/s and 0.6 m/s, respectively. Thus, the adopted numerical model is sufficiently reliable and will be applied for further investigations.

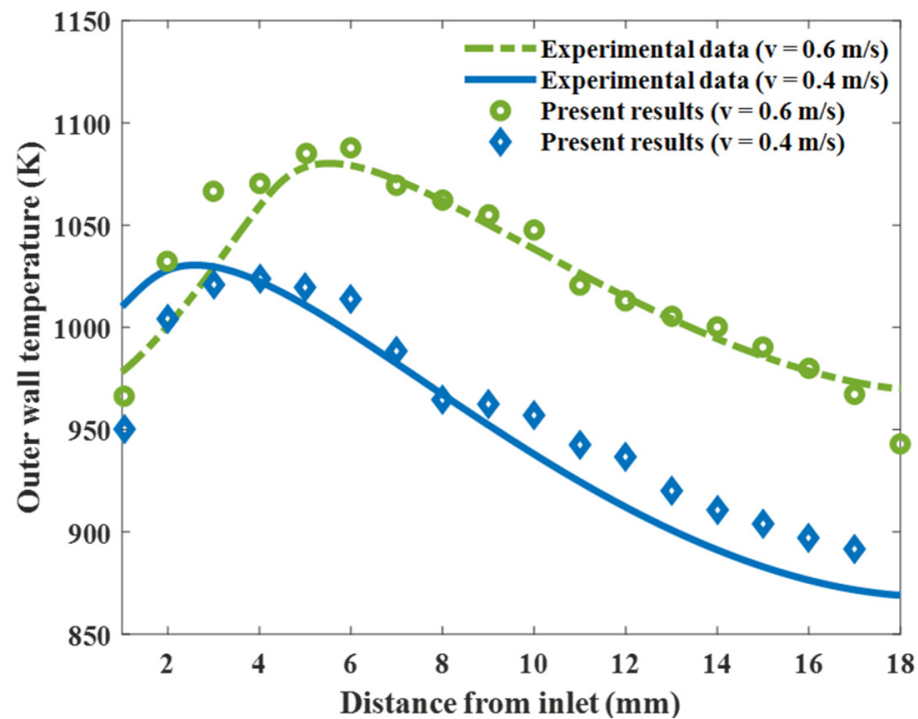


Figure 3. Comparison of the centerline temperature profiles between the experimental [27] and the present results on the outer wall of the micro-combustor at $\phi = 1.0$.

3. Results and Discussion

3.1. Effect of the Cavity Axial Location x_c

A parametric study of the cavity axial location (x_c) has been conducted to evaluate the effect on the temperature distribution of the combustor and then compare it with the conventional combustor. The conventional combustor without any cavity is considered the reference case. For simplicity and comparison, the cavity axial location x_c is normalized by the total length of the combustor L , i.e., x_c/L . Figure 4 compares the outer-wall temperature distribution of the micro-conventional combustor (Figure 4a) and the micro-cavity combustor at various x_c/L , with $x_c/L = 1/9$ (Figure 4b), $2/9$ (Figure 4c), $3/9$ (Figure 4d), $4/9$ (Figure 4e), respectively, where the inlet velocity is set to 0.8 m/s, as the methane/air equivalence ratio is kept at 1.0. It is shown that a high-temperature zone at (Figure 4a) forms close to the downstream, indicating that the chemical reaction shifts downstream. However, in the presence of a cavity, the flame location shifts upstream.

To shed light on how the cavity implementation affects the temperature distribution of the outer wall, the flame temperature distribution at the $y = 0$ plane is studied, as shown in Figure 5. It is seen that the high-temperature zone is dramatically expanded and concentrated very close to the inlet at Figure 5b in comparison to the reference. The cavity location contributes to the effect of temperature, and velocity in the $y = 0$ plane can be observed in Figure 5. The addition of the cavity increases the contact area and alters the heat transfer direction between the fluid and the solid. It should be noted that the location of the cavity, as shown in Figure 5b, forms a backflow region, which not only preheats the incoming flow but also enhances heat recirculation. Finally, the cavity, as depicted in Figure 5d,e, shows a similar result to the reference because the fuel and oxidant have been consumed in the upstream region, so the cavity axial location has a negligible effect on the heat transfer. This phenomenon can be understood by explaining the heat transfer direction in the micro-cavity combustor, as shown in Figure 6. The mixture gas combusts in the channel and releases an amount of heat; then the solid wall absorbs the heat and conducts it to the upstream wall, which preheats the other mixture gas.

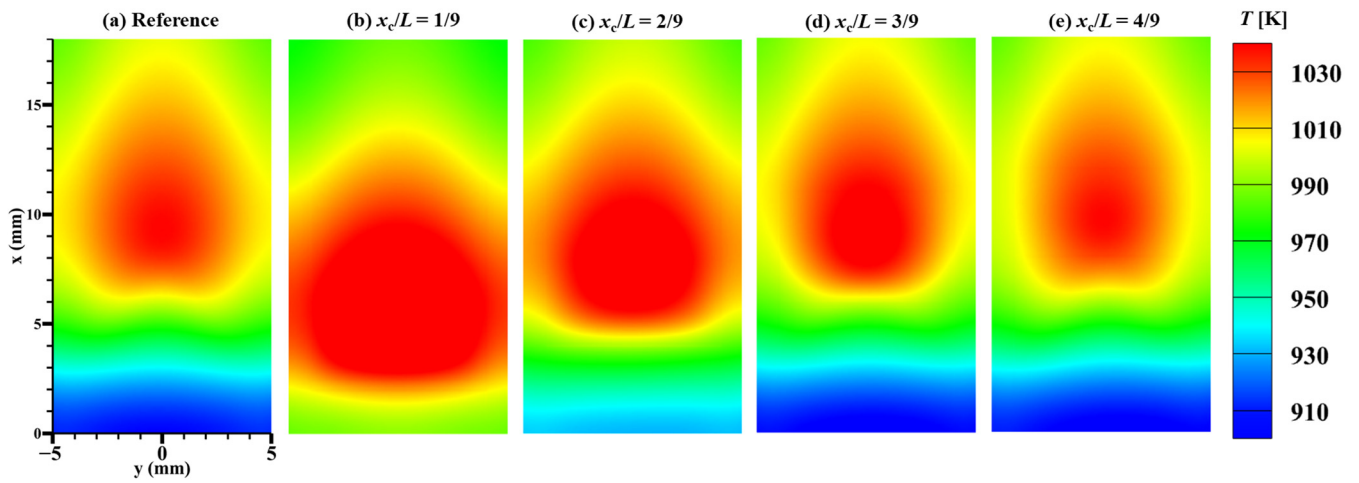


Figure 4. A comparison of the outer-wall temperature contours between the reference case and the combustors with a cavity but placed at various dimensionless axial locations x_c/L , as the inlet velocity and the equivalence ratio are set to 0.8 m/s and 1.0, respectively.

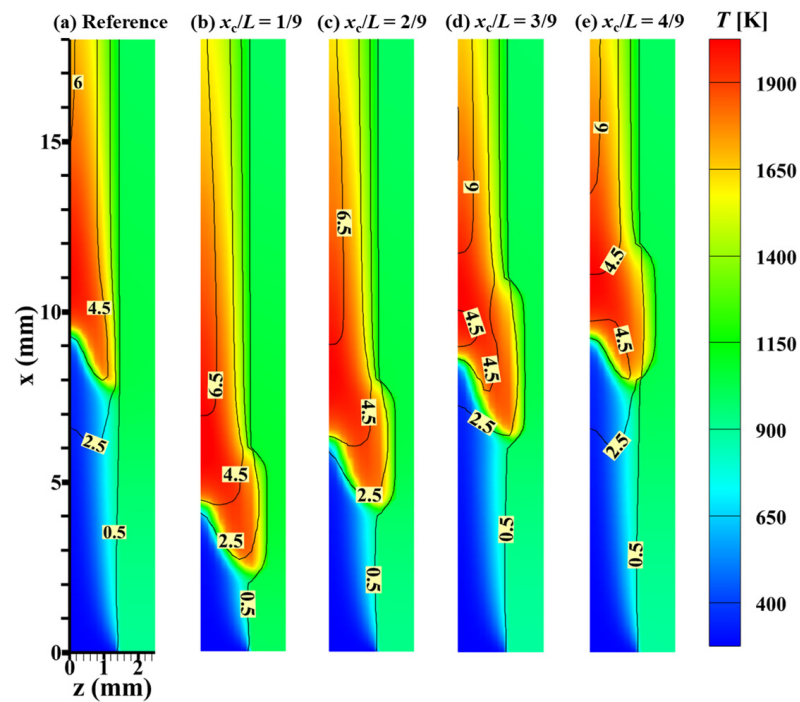


Figure 5. The predicted center-plane temperature contours at $y = 0$ plane with iso-velocity lines, where the inlet velocity and the equivalence ratio are set at 0.8 m/s and 1.0, respectively.

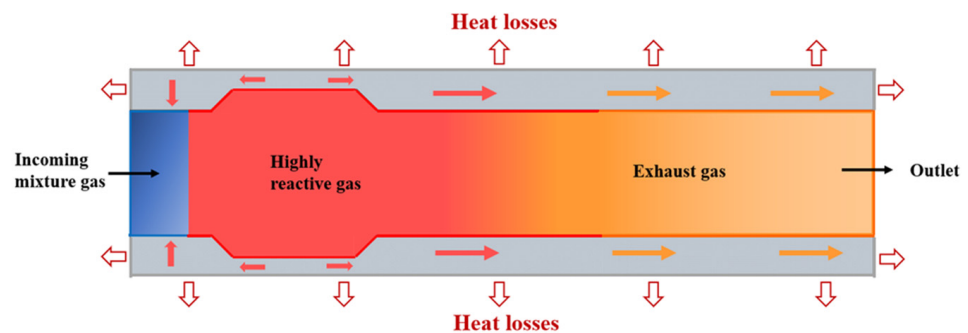


Figure 6. Heat transfer diagram of the micro-cavity combustor.

To quantify the influence of the cavity dimensionless axial location on the thermal performance of the micro-combustor, the outer-wall mean temperature (OWMT) is plotted as a function of the inlet velocity and the cavity dimensionless axial location shown in Figure 7a. At the inlet velocity of 0.4 m/s, the OWMTs are highly overlapped. This is because the fuel and oxidant have a sufficient residence time to combust and transfer heat to the combustor wall due to the relatively low inlet velocity. On the contrary, as the velocity increases, the advantage of adding a cavity to the combustor is revealed. The difference in the OWMT between the combustor with the cavity location of $x_c/L = 1/9$ and reference is up to 64.8 K at the highest inlet velocity (1.0 m/s), indicating that the cavity axial location is critical to OWMT.

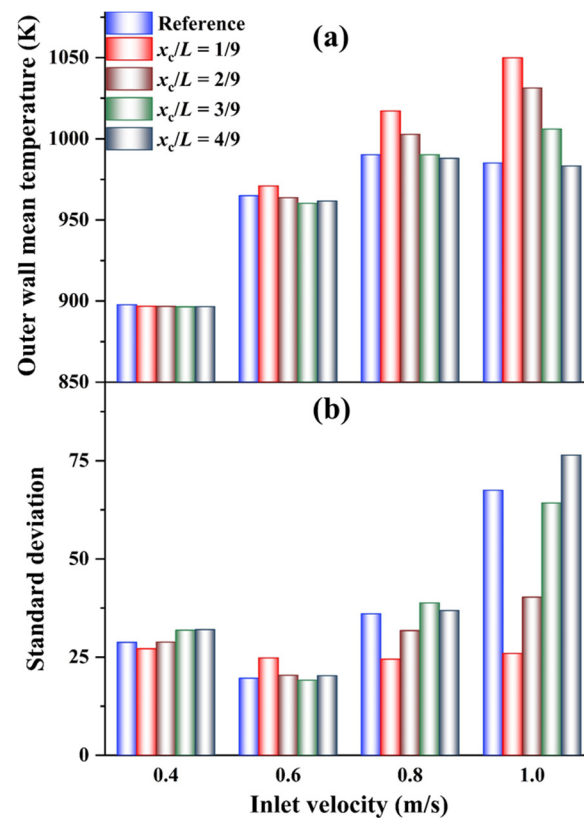


Figure 7. Comparison of the outer wall mean temperature (OWMT) (a) and standard deviation (b) under various inlet velocities and different cavity dimensionless axial locations x_c/L , as the methane/air equivalence ratio ϕ is set to 1.0.

As far as the heat transfer performance is concerned, the standard deviation of the wall temperature is essential to be analyzed. Note that the standard deviation indicates the uniformity and difference of the temperature variation. The standard deviation refers to the temperature deviation of maximum and minimum temperatures, and hence a lower standard deviation is desirable, which represents a more concentrated temperature distribution. In Figure 7, the fuel-oxidizer equivalence ratio for all cases is set to be 1.0. This means that all the chemical reaction is complete. In theory, a higher inlet velocity is associated with a larger chemical energy input. Thus, it is reasonable to assume that a higher inlet velocity is accompanied by a higher outer wall mean temperature arising from the larger reaction heat. Figure 7b illustrates the standard deviation of the outer wall static temperature as a function of the cavity dimensionless axial location and the inlet velocity, as the equivalence ratio ϕ is set to 1.0. Comparing Figure 7a,b reveals that the maximum mean temperature and the lowest standard deviation appear at $x_c/L = 1/9$, so the optimized cavity location is found. The underlying mechanism behind this phenomenon is that, when the cavity is placed closer to the combustor inlet, it helps the gas mixture to form a backflow

region and preheat the incoming fluid, thus increasing the maximum temperature. To summarize, the axial location of the cavity plays an important role both in the wall mean temperature as well as uniformity.

3.2. Effect of the Cavity Volume V_c

According to the previous section, the optimized dimensionless cavity axial location x_c/L is at $1/9$. Based on this optimum location, further improvement of thermal performances has been focused on altering the cavity volume, which could be changed via three parameters: (1) the horizontal length (L_c), (2) the vertical depth (H_c) and (3) the incline angle (θ_c). Considering that the fluid volume could be varied due to the change in the cavity structure, it is important to calculate the cavity volume V_c . It can be determined as

$$V_c = \left(L_c + \frac{H_c}{\tan(\theta_c)} \right) \cdot H_c \cdot W_c \quad (10)$$

The dimensionless cavity length L_{c_dims} with respect to x-direction is derived below:

$$L_{c_dims} = \frac{L_c}{L} \quad (11)$$

The dimensionless cavity height H_{c_dims} with respect to z-direction is derived below

$$H_{c_dims} = \frac{2 \cdot H_c}{H - 2 \cdot T} \quad (12)$$

The axial location and the bottom horizontal length do not change when we conduct a parametric study with respect to the incline angle θ_c . The detailed ranges of these three parameters involved in the cavity dimensions are listed in Table 3.

Table 3. The parameters of cavity volume.

Cavity Volume V_c (mm ³)	L_c (mm)	H_c (mm)	θ_c (°)	W_c (mm)
$0 < V_c \leq 22$	$0 < L_c \leq 5$	$0 < H_c \leq 0.5$	$15 \leq \theta_c \leq 75$	8
$V_c = 0$ (Reference case)	0	0	0	0

3.2.1. Variation of the Cavity Height H_{c_dims}

The OWMT and standard deviation under various inlet velocities and cavity heights (H_c)—where the cavity is located at $x_c/L = 1/9$ and the equivalence ratio is set to be 1.0—are shown in Figure 8. At a low inlet velocity, the thermal performance tends to have a negligible difference. With increasing the inlet velocity, the OWMT increases. Additionally, the OWMT with the cavity height of $1/3$ is the highest among the three configurations at the inlet velocity of 1.0 m/s. On the contrary, the OWMT is the lowest at the cavity height of $1/15$ mm, and the flame starts to become unstable, which has an extremely high standard deviation. To get a more comprehensive understanding of the flame characteristics, a center-plane temperature contour with iso-velocity at the inlet velocity of 0.8 m/s is shown in Figure 9. The highest temperature zone located near the inlet at the cavity height is set to $1/5$ and $1/3$. However, the highest temperature zone shifts downstream at the cavity height of $1/15$. It should be noted that increasing the cavity height is associated with an increase in the contact area between the combustion fluid and the solid wall. Thus, the residence time and the heat exchange between the combustion fluid and the solid wall are increased. Therefore, increasing the cavity height can enhance the heat transfer effect, thereby resulting in a more uniform temperature distribution, which can be expressed as a low standard deviation. Additionally, though the cavity height of $H_{c_dims} = 1/5$ is the critical height H_{cc} of the micro-combustor and is sufficient enough to get a satisfactory

thermal performance, the minor difference between the cavity height of 1/5 and 1/3 with a higher inlet velocity still needs to be further analyzed.

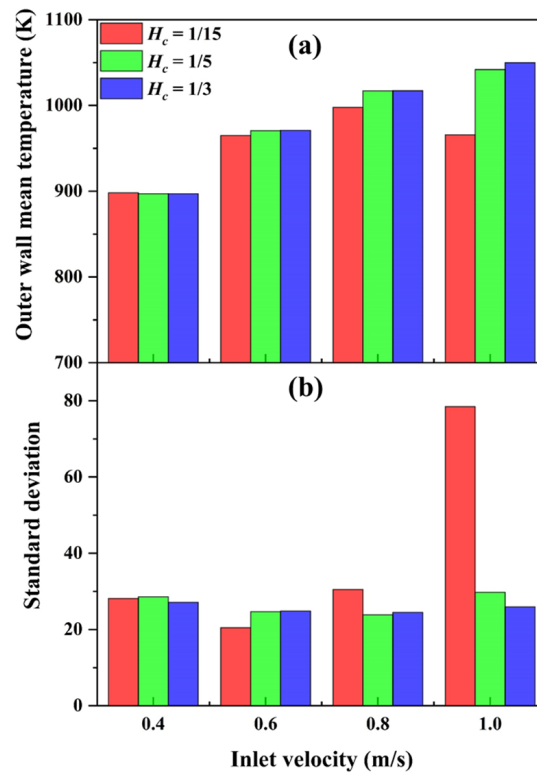


Figure 8. Predicted outer-wall mean temperature (OWMT) (a) and standard deviation (b) under various inlet velocities and cavity heights H_c , as $x_c/L = 1/9$ and $\phi = 1.0$.

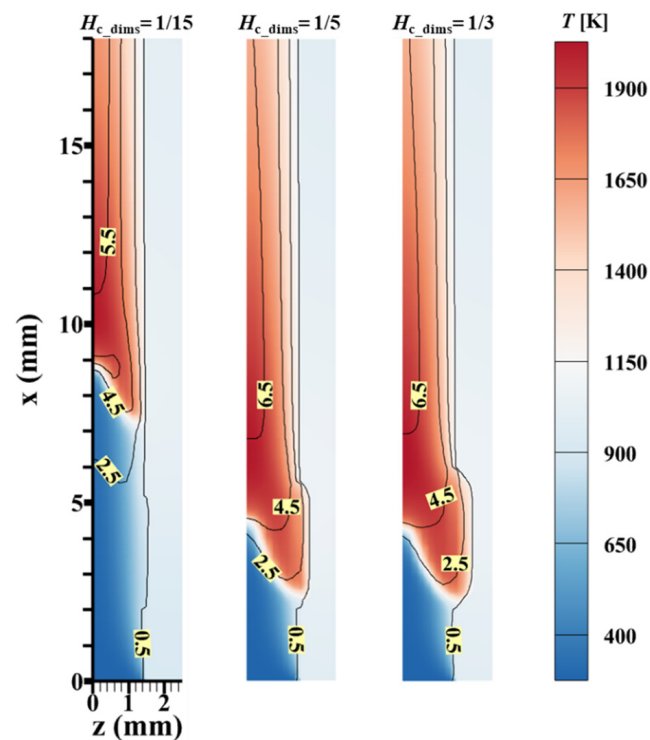


Figure 9. Center-plane temperature contour at $y = 0$ plane with iso-velocity lines under various cavity heights H_c , as $x_c/L = 1/9$, $v = 0.8$ m/s, and $\phi = 1.0$.

The centerline temperature distribution of three cavity heights at the outer wall along the axial direction under the inlet velocities of 0.8 m/s and 1.0 m/s is indicated in Figure 10. When the inlet velocity is increased, the highest temperature regions are found to be shifted downstream at three inlet velocities. The highest temperature is close to the outlet at a low cavity height (1/15). As the cavity height is increased, the highest temperature is closer to the inlet, and the gap between the start and end points is getting smaller, which also indicates the temperature distribution is more uniform with a higher cavity height.

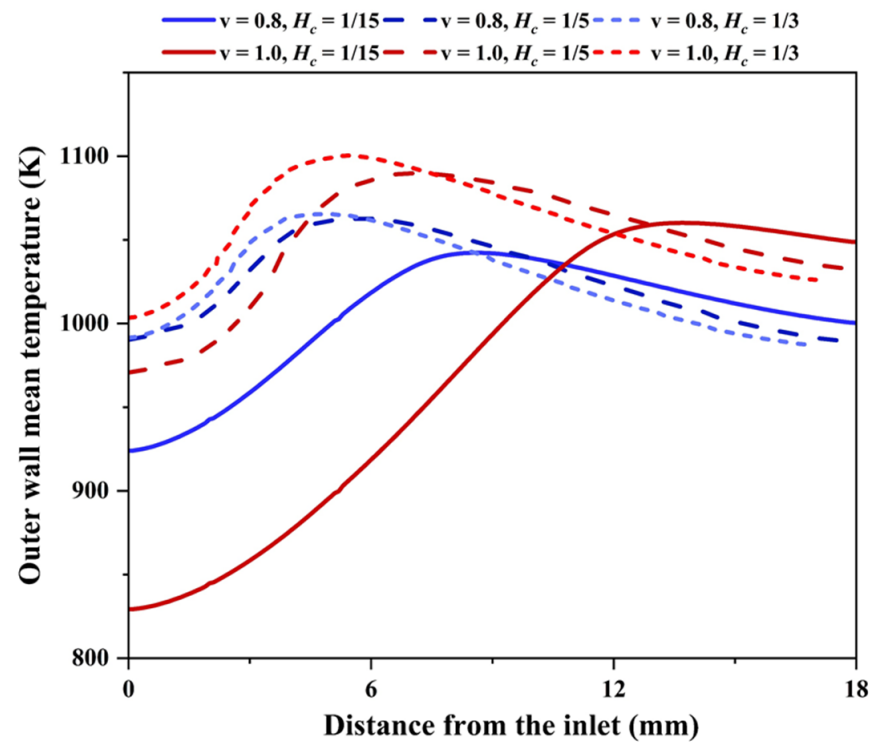


Figure 10. The distribution of the centerline temperature at the outer wall along the axial direction under varies inlet velocity and dimensionless cavity heights (H_{c_dims}), where $x_c/L = 1/9$ and $\phi = 1.0$.

3.2.2. Variations of θ_c and L_c

Table 4 summarizes the OWMT and standard deviation under various inlet velocities, cavity lengths (1/18, 3/18 and 5/18) and cavity angles (15° , 45° and 75°). It can be seen that there is a negligible difference in the calculated wall temperature and its standard deviation, as the cavity height and angle are varied. This suggests that the effect of these combustor parameters on the thermal performance can be neglected, but the cavity height should be given sufficient consideration when attempting to optimize the combustor working performance.

3.3. Effect of the Equivalence Ratio ϕ

Now the effect of the equivalence ratio on the thermal performance of the micro-cavity combustor is investigated. Figure 11 shows the outer wall temperature contours under various equivalence ratios (0.9, 1.0, 1.1), where the inlet velocity and the cavity dimensionless axial location are set to be 0.8 m/s and 1/9, respectively. It can be observed that the high-temperature region at the equivalence ratio of 1.0 is the largest, followed by the case with $\phi = 1.1$ and 0.9. This is due to the fact that for off-stoichiometric conditions, either the fuel or the oxidant is not sufficient to sustain combustion. Furthermore, it is worth mentioning that a slightly fuel-rich condition is more desirable compared to a slightly fuel-lean condition for maximizing thermal performance.

Table 4. Mean temperature and standard deviation of the outer wall under various inlet velocities, cavity lengths (L_c) and cavity angles (θ_c), where $x_c/L = 1/9$ and $\phi = 1.0$.

Inlet Velocity (m/s)	Outer Wall Mean Temperature (K) (Upper Values) Standard Deviation (Lower Values)					
	$L_c = 1/18$	$L_c = 3/18$	$L_c = 5/18$	$\theta_c = 15^\circ$	$\theta_c = 45^\circ$	$\theta_c = 75^\circ$
0.4	899.2	896.9	898.1	899.0	896.9	897.6
	28.5	27.1	28.1	27.7	27.1	27.7
0.6	970.2	970.9	970.1	968.3	970.9	970.1
	25.1	24.8	24.7	23.0	24.8	25.0
0.8	1017.6	1017.2	1016.4	1013.0	1017.2	1017.2
	24.3	24.4	24.3	23.8	24.4	24.9
1.0	1048.2	1049.9	1050.4	1045.5	1049.9	1050.1
	25.4	25.9	25.8	27.2	25.9	26.1

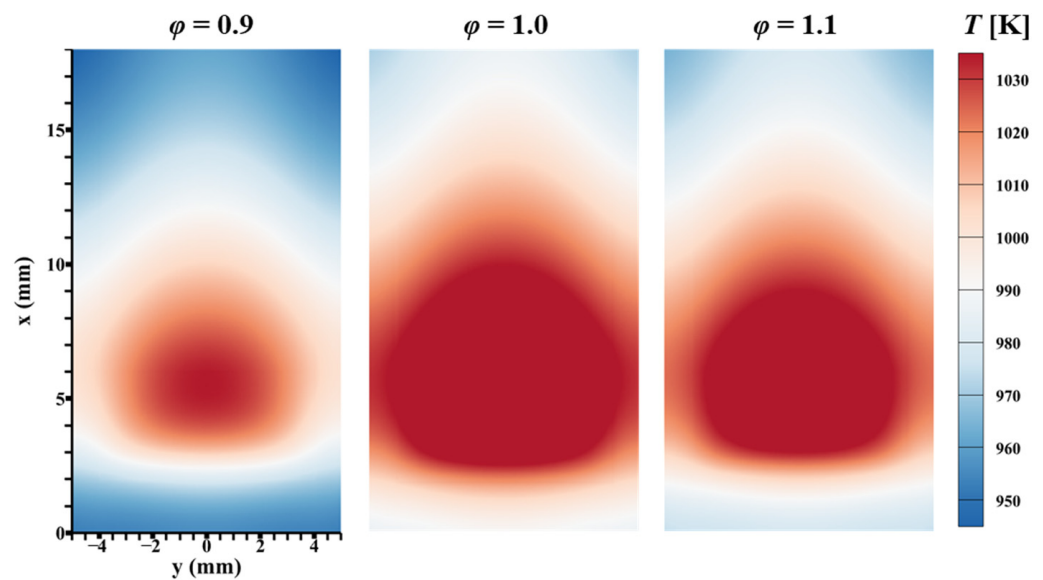


Figure 11. Outer wall temperature contour under various equivalence ratios, where $v = 0.8$ m/s.

To quantify the observed phenomena in Figure 11, the centerline temperature distribution variations on the outer wall under various equivalence ratios and inlet velocities along the axial direction are shown in Figure 12. It can be seen that the centerline temperature of the outer wall at $\phi = 0.9$ is significantly lower than that of those at $\phi = 1.0$ and 1.1 cases, no matter what the inlet velocity is set to. This is consistent with the results presented in Figure 11. Another observation from Figure 12 is that, as the inlet velocity is increased, the centerline temperature is also elevated due to the increased chemical energy input, and the flame is approaching downstream.

To provide insights into the response of the wall temperature and the temperature uniformity to the equivalence ratio, Figure 13 shows the OWMT and standard deviation as a function of the cavity axial location at the inlet velocity of 0.8 m/s. It is noted that, for a given equivalence ratio, OWMT decreases as the cavity is placed further downstream. This is due to the fact that the presence of a cavity near the combustor inlet is more advantageous for transferring heat from the gas phase to the solid phase. In addition, it can be observed that regardless of where the cavity is located, OWMT exhibits a non-monotonical trend with the equivalence ratio. Specifically, it increases first and then decreases as the mixture is varied from lean to rich conditions. On the other hand, this is not the case for the calculated temperature standard deviation. At a relatively small x_c/L , there is little difference in the standard deviation with the equivalence ratio. However, as the cavity is placed at $x_c/L = 3/9$, the outer temperature at $\phi = 0.9$ tends to be the most non-uniform. Therefore,

it can be concluded that the optimized cavity location is at $1/9$ in terms of the OWMT and the standard deviation. Next, when comparing the equivalence ratio at different cavity locations, the worst and best mean temperatures and standard deviation remain at $\phi = 0.9$, and 1.0 , respectively. While the best cavity location occurs at $x_c/L = 1/9$ at all equivalence ratios. In addition, when the cavity location is closer to the inlet, the thermal performance is better, and the cavity appears to have no influence on the thermal performance at and after $4/9$. Therefore, the outer wall temperature variation at $1/9$ is found to be the smallest and the highest amount of heat released during the combustion process.

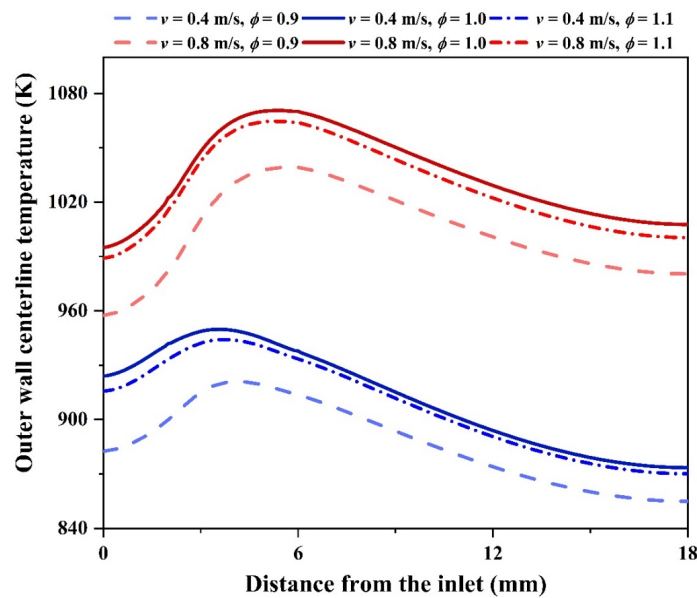


Figure 12. The distribution of the centerline temperature at the outer wall along the axial direction under various inlet velocities and equivalence ratios, where $x_c/L = 1/9$.

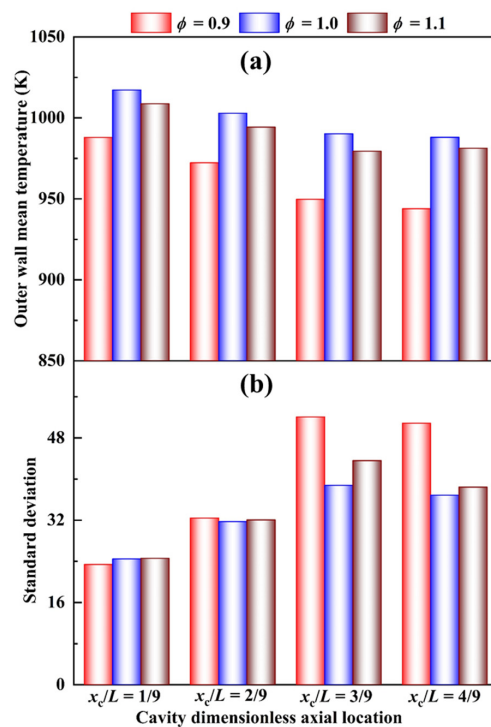


Figure 13. Outer wall mean temperature (OWMT) (a) and standard deviation (b) under various x_c/L and equivalence ratio ϕ .

4. Further Exergy Generation Investigations

In this section, the effect of the cavity on exergy [50] generation from the micro-combustion system is analyzed. According to the second law of thermodynamics, the exergy energy efficiency is derived as below:

$$Ex_{in} = \dot{m}_{CH_4} \times Q_{LHV}, \quad (13)$$

where Ex_{in} is the inlet exergy; \dot{m}_{CH_4} is the methane mass flow rate; and Q_{LHV} is the lower heating value of the methane (50.0 MJ/kg)

Since the outlet pressure of the combustion system is equal to the atmospheric pressure, the equation of the total exergy loss can be simplified below

$$Ex_{eg} = Ex_{loss} + \dot{m}_{inlet} \times T_{\infty} \times \left(c_{p_{outlet}} \ln \frac{T_{\infty}}{T_{eg}} \right), \quad (14)$$

where Ex_{eg} is the total exergy loss at the outlet; Ex_{loss} is the exergy of the exhaust gas; \dot{m}_{inlet} is the inlet mass flow rate; T_{∞} is the ambient temperature; and T_{eg} is the exhaust gas temperature.

$$Ex_{des} = Ex_{in} - Ex_{eg}, \quad (15)$$

where Ex_{des} is the exergy utilization during the combustion process.

$$\eta_{exergy} = \left(1 - \frac{Ex_{des}}{Ex_{in}} \right) \times 100\%, \quad (16)$$

where η_{exergy} is the exergy efficiency.

Figure 14 shows a comparison of calculated exergy efficiency between the conventional micro-combustor and micro-cavity combustor at $x_c/L = 1/9$. The results indicate that the exergy is decreased with increasing the inlet velocity, regardless of with or without the cavity. Furthermore, the exergy efficiency difference between the conventional combustor (i.e., the reference case) and the proposed combustors with cavities is increased with increasing inlet velocity. To be more specific, the exergy efficiency is almost the same at the inlet velocity of 0.4 m/s, and the highest exergy efficiency difference is 9.8% at the inlet velocity of 1.0 m/s. The reason for this phenomenon is that the outlet temperature in the combustor with a cavity is reduced minimally at a low inlet velocity but reduced significantly at a high inlet velocity. Therefore, adding the cavity in the micro-combustor helps to reduce the outlet temperature of exhaust gas due to the positive effect on enhancing the heat transfer from the combustion channel to the solid wall, hence increasing the exergy efficiency.

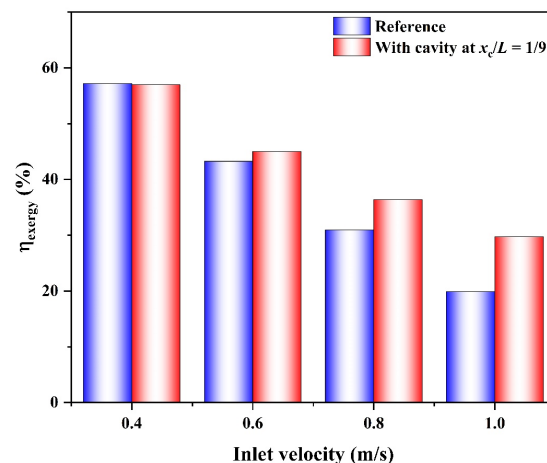


Figure 14. A comparison between the conventional micro-combustor (reference) and micro-cavity combustor at $x_c/L = 1/9$ location under various inlet velocities with $\phi = 1.0$.

5. Effect of Blending Methane with Hydrogen

In this section, the effect of blending hydrogen with methane on the exergy and thermal performances of the micro-combustor with cavities is examined, as the equivalence ratio and the axial dimensionless location x_c/L are kept at 1.0 and 1/9, respectively. The hydrogen blended ratio α is defined below:

$$\alpha = \frac{V_{H_2}}{V_{H_2} + V_{CH_4}} \times 100\%, \quad (17)$$

where V_{H_2} is the volume fraction of the hydrogen and V_{CH_4} is the volume fraction of the methane.

The centerline temperature distributions at the outer wall with hydrogen additions of 25% and 50% are compared with pure methane (100% CH_4 + 0% H_2), as shown in Figure 15. The results reveal that a higher α has a positive impact on locating the high-temperature region near the inlet, regardless of the inlet velocities. This is advantageous in terms of promoting flame stability [86] in practical combustion systems. On the other hand, the OWMT is shown to be decreased rapidly with increasing hydrogen addition α , whatever the inlet velocity is set to. The underlying mechanism for this phenomenon is that, when the same amount of volume fraction of methane is replaced with hydrogen, the total chemical energy input is reduced because of the relatively low volumetric energy density of hydrogen.

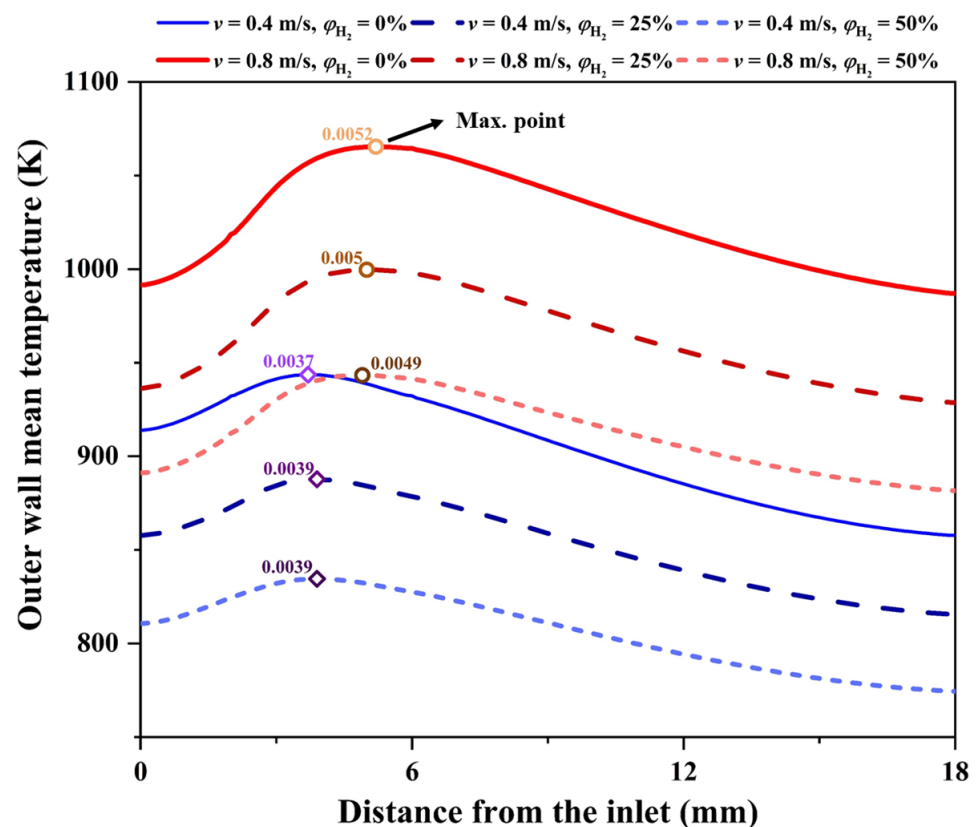


Figure 15. The distribution of the centerline temperature at the outer wall along the axial direction under various inlet velocities and hydrogen fractions, where $x_c/L = 1/9$ and $\phi = 1.0$.

Figure 16 compares the variation of the exergy efficiency and the standard deviation of outer walls at different blending ratios and inlet velocities. It can be seen from Figure 16a that η_{exergy} of the micro-combustor in the presence of hydrogen is generally lower compared to that of the pure methane case. Furthermore, it should be noted that there is a negligible difference in the calculated η_{exergy} with hydrogen added. Figure 16b

indicates that the temperature standard deviation of the outer walls exhibits a monotonic trend with the hydrogen blended ratio. That is, a higher blended ratio leads to a low value of the standard deviation. This means that the presence of hydrogen is beneficial to improving the temperature uniformity of the combustor outer wall. This phenomenon is desirable in practical power generation systems like the MTPV system. A comparison of Figures 15 and 16 reveals that hydrogen addition plays a negative role in lowering OWMT but has a positive effect on enhancing temperature uniformity.

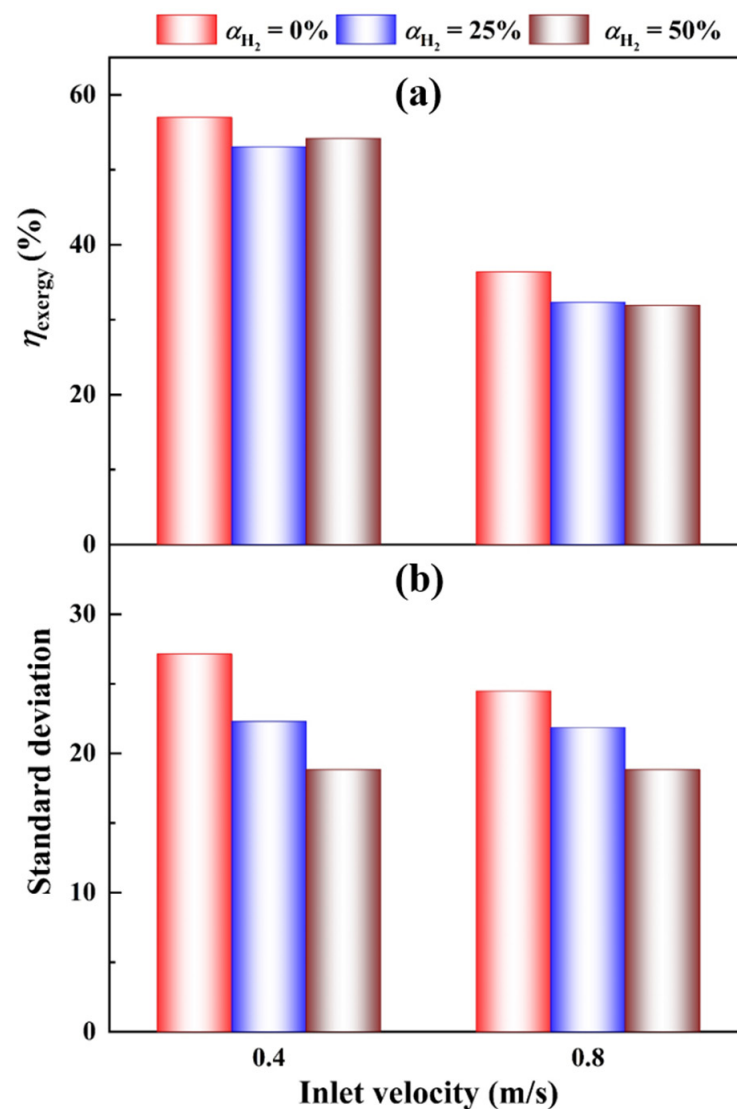


Figure 16. The exergy efficiency (a) and standard deviation (b) at $x_c/L = 1/9$ location under various inlet velocities and hydrogen blended ratios.

6. Discussion and Conclusions

In this work, a detailed three-dimensional, time-domain, computational model is established to evaluate the effect of implementing a cavity in a methane-air-fueled micro-combustor on enhancing thermal performances, thermodynamics and exergy efficiency. The developed model is first validated with the experimental data in the literature. Then it is used to explore the effects of (1) the cavity axial location, (2) the cavity volume and (3) the equivalence ratio on improving the outer wall mean temperature (OWMT), exergy efficiency η_{exergy} . The key findings are summarized below:

1. The presence of the cavity gives rises to more uniform temperature distribution and an increase in the OWMT by approximately 64.8 K. This is due to the fact that the

cavity contributes to anchoring the high-temperature zone in the upstream location, especially at high inlet velocity, thus enhancing the heat transfer between the gas phase and solid phase as well as preheating the fresh mixture.

2. The cavity height H_c plays a critical role in determining the thermal performance of the combustor. However, the effects of the cavity length L_c and angle θ_c are negligible. There exists a critical cavity height H_{cc} with a value of $\frac{1}{5}$, above which the OWMT and temperature uniformity are less affected.
3. The OWMT is found to increase with increasing inlet velocity, regardless of the equivalence ratio ϕ . The optimal equivalence ratio ϕ_{opt} corresponds to the maximum outer wall temperature, and the most uniform temperature distribution is 1.0.
4. The exergy efficiency analysis reveals a monotonic trend with the inlet velocity, i.e., a higher inlet velocity and lower exergy efficiency. The implementation of the cavity is found to lead to an increase in the exergy efficiency by up to 9.8% compared to the conventional combustor in the absence of any cavity.
5. The hydrogen addition plays a negative role in affecting OWMT and exergy efficiency, but it significantly enhances temperature uniformity.

Generally, the present work demonstrates that implementing a cavity with a proper structure and optimum volume design is a simple but effective way to enhance the thermal performances of micro-combustors and to improve thermodynamic/exergy efficiency.

Author Contributions: J.T.: Conceptualization, Software, Methodology, Validation, Formal analysis, Writing—original draft. T.C.: Supervision, Review & Editing. All authors have read and agreed to the published version of the manuscript.

Funding: This research received no external funding.

Data Availability Statement: The data supporting this present work are available from the corresponding author upon reasonable request.

Acknowledgments: We gratefully acknowledge the academic support and guidance provided by Dan Zhao from the University of Canterbury.

Conflicts of Interest: The authors declare no conflict of interest.

References

1. Mustafa, K.F.; Abdullah, S.; Abdullah, M.Z.; Sopian, K. A review of combustion-driven thermoelectric (TE) and thermophotovoltaic (TPV) power systems. *Renew. Sustain. Energy Rev.* **2017**, *71*, 572–584. [\[CrossRef\]](#)
2. Han, L.; Li, J.; Zhao, D.; Cai, T.; Wang, N. Energy and exergy conversion enhancement of a premixed hydrogen-fuelled wavy-combustor for micro-thermophotovoltaic application. *Appl. Therm. Eng.* **2021**, *196*, 117328. [\[CrossRef\]](#)
3. Cao, H.L.; Xu, J.L. Thermal performance of a micro-combustor for micro-gas turbine system. *Energy Convers. Manag.* **2007**, *48*, 1569–1578. [\[CrossRef\]](#)
4. Enagi, I.I.; Al-attab, K.A.; Zainal, Z.A. Combustion chamber design and performance for micro gas turbine application. *Fuel Process. Technol.* **2017**, *166*, 258–268. [\[CrossRef\]](#)
5. Kundu, A.; Jang, J.H.; Gil, J.H.; Jung, C.R.; Lee, H.R.; Kim, S.H.; Ku, B.; Oh, Y.S. Micro-fuel cells—Current development and applications. *J. Power Sources* **2007**, *170*, 67–78. [\[CrossRef\]](#)
6. Zhao, D.; Ji, C.; Teo, C.; Li, S. Performance of small-scale bladeless electromagnetic energy harvesters driven by water or air. *Energy* **2014**, *74*, 99–108. [\[CrossRef\]](#)
7. Ju, Y.; Maruta, K. Microscale combustion: Technology development and fundamental research. *Prog. Energy Combust. Sci.* **2011**, *37*, 669–715. [\[CrossRef\]](#)
8. Yang, W.; Jiang, D.; Kenny, C.K.Y.; Zhao, D.; Pang, J. Combustion process and entropy generation in a novel microcombustor with a block insert. *Chem. Eng. J.* **2015**, *274*, 231–237.
9. Li, S.; Zhao, D. Heat flux and acoustic power in a convection-driven T-shaped thermoacoustic system. *Energy Convers. Manag.* **2013**, *75*, 336–347. [\[CrossRef\]](#)
10. Ji, C.; Zhao, D. Two-dimensional lattice Boltzmann investigation of sound absorption of perforated orifices with different geometric shapes. *Aerosp. Sci. Technol.* **2014**, *39*, 40–47. [\[CrossRef\]](#)
11. Zhao, D.; Li, S.; Yang, W.; Zhang, Z. Numerical investigation of the effect of distributed heat sources on heat-to-sound conversion in a T-shaped thermoacoustic system. *Appl. Energy* **2015**, *144*, 204–213. [\[CrossRef\]](#)
12. Zhao, D.; Reyhanoglu, M. Feedback control of acoustic disturbance transient growth in triggering thermoacoustic instability. *J. Sound Vib.* **2014**, *333*, 3639–3656. [\[CrossRef\]](#)

13. Rubio-Hervas, J.; Zhao, D.; Reyhanoglu, M. Nonlinear feedback control of self-sustained thermoacoustic oscillations. *Aerosp. Sci. Technol.* **2015**, *41*, 209–215. [[CrossRef](#)]
14. Zhao, D.; Gutmark, E.; Reinecke, A. Mitigating self-excited flame pulsating and thermoacoustic oscillations using perforated liners. *Sci. Bull.* **2019**, *64*, 941–952. [[CrossRef](#)]
15. Duan, X.; Fu, J.; Zhang, Z.; Liu, J.; Zhao, D.; Zhu, G. Experimental study on the energy flow of a gasoline-powered vehicle under the NEDC of cold starting. *Appl. Therm. Eng.* **2017**, *115*, 1173–1186. [[CrossRef](#)]
16. Li, J.; Chou, S.K.; Li, Z.W.; Yang, W.M. Characterization of wall temperature and radiation power through cylindrical dump micro-combustors. *Combust. Flame* **2009**, *156*, 1587–1593. [[CrossRef](#)]
17. Cai, T.; Tang, A.; Zhao, D.; Zhou, C.; Huang, Q. Experimental observation and numerical study on flame structures, blowout limit and radiant efficiency of premixed methane/air in micro-scale planar combustors. *Appl. Therm. Eng.* **2019**, *158*, 113810. [[CrossRef](#)]
18. Han, L.; Li, J.; Zhao, D.; Xi, Y.; Gu, X.; Wang, N. Effect analysis on energy conversion enhancement and NO_x emission reduction of ammonia/hydrogen fuelled wavy micro-combustor for micro-thermophotovoltaic application. *Fuel* **2021**, *289*, 119755. [[CrossRef](#)]
19. Li, L.; Zhao, D. Prediction of stability behaviors of longitudinal and circumferential eigenmodes in a choked thermoacoustic combustor. *Aerosp. Sci. Technol.* **2015**, *46*, 12–21. [[CrossRef](#)]
20. Chen, S.; Zhao, D. Numerical study of non-reacting flowfields of a swirling trapped vortex ramjet combustor. *Aerosp. Sci. Technol.* **2018**, *74*, 81–92. [[CrossRef](#)]
21. Sun, Y.; Rao, Z.; Zhao, D.; Wang, B.; Sun, D.; Sun, X. Characterizing nonlinear dynamic features of self-sustained thermoacoustic oscillations in a premixed swirling combustor. *Appl. Energy* **2020**, *264*, 114698. [[CrossRef](#)]
22. Yan, Y.; Zhang, C.; Gao, J.; Shen, K.; Gao, W. Numerical study on premixed hydrogen/air combustion characteristics and heat transfer enhancement of micro-combustor embedded with pin fins. *Int. J. Hydrogen Energy* **2021**, *46*, 38519–38534. [[CrossRef](#)]
23. Chia, L.C.; Feng, B. The development of a micropower (micro-thermophotovoltaic) device. *J. Power Sources* **2007**, *165*, 455–480. [[CrossRef](#)]
24. Cai, T.; Zhao, D. Enhancing and assessing ammonia-air combustion performance by blending with dimethyl ether. *Renew. Sustain. Energy Rev.* **2022**, *156*, 112003. [[CrossRef](#)]
25. Cai, T.; Zhao, D.; Chan, S.H.; Shahsavari, M. Tailoring reduced mechanisms for predicting flame propagation and ignition characteristics in ammonia and ammonia/hydrogen mixtures. *Energy* **2022**, *260*, 125090. [[CrossRef](#)]
26. Yan, Y.; Tang, W.; Zhang, L.; Pan, W.; Yang, Z.; Chen, Y.; Lin, J. Numerical simulation of the effect of hydrogen addition fraction on catalytic micro-combustion characteristics of methane-air. *Int. J. Hydrogen Energy* **2014**, *39*, 1864–1873. [[CrossRef](#)]
27. Tang, A.; Xu, Y.; Pan, J.; Yang, W.; Jiang, D.; Lu, Q. Combustion characteristics and performance evaluation of premixed methane/air with hydrogen addition in a micro-planar combustor. *Chem. Eng. Sci.* **2015**, *131*, 235–242. [[CrossRef](#)]
28. Tang, A.; Deng, J.; Cai, T.; Xu, Y.; Pan, J. Combustion characteristics of premixed propane/hydrogen/air in the micro-planar combustor with different channel-heights. *Appl. Energy* **2017**, *203*, 635–642. [[CrossRef](#)]
29. Sun, Y.; Zhao, D.; Cai, T. Dilution effect on thermal performances and NO emission characteristics of an ammonia-oxygen micro-thermophotovoltaic system. *Therm. Sci. Eng. Prog.* **2022**, *34*, 101401. [[CrossRef](#)]
30. Cai, T.; Zhao, D.; Li, X.; Shi, B.; Li, J. Mitigating NO_x emissions from an ammonia-fueled micro-power system with a perforated plate implemented. *J. Hazard. Mater.* **2021**, *401*, 123848. [[CrossRef](#)]
31. Cai, T.; Zhao, D.; Sun, Y.; Ni, S.; Li, W.; Guan, D.; Wang, B. Evaluation of NO emissions characteristics in a CO₂-free micro-power system by implementing a perforated plate. *Renew. Sustain. Energy Rev.* **2021**, *145*, 111150. [[CrossRef](#)]
32. Juangsa, F.B.; Darmanto, P.S.; Aziz, M. CO₂-free power generation employing integrated ammonia decomposition and hydrogen combustion-based combined cycle. *Therm. Sci. Eng. Prog.* **2020**, *19*, 100672. [[CrossRef](#)]
33. Zheng, S.; Liu, H.; Sui, R.; Zhou, B.; Lu, Q. Effects of radiation reabsorption on laminar NH₃/H₂/air flames. *Combust. Flame* **2022**, *235*, 111699. [[CrossRef](#)]
34. Wierzbicki, T.A.; Lee, I.C.; Gupta, A.K. Combustion of propane with Pt and Rh catalysts in a meso-scale heat recirculating combustor. *Appl. Energy* **2014**, *130*, 350–356. [[CrossRef](#)]
35. Wang, Y.; Zhou, Z.; Yang, W.; Zhou, J.; Liu, J.; Wang, Z.; Cen, K. Combustion of hydrogen-air in micro combustors with catalytic Pt layer. *Energy Convers. Manag.* **2010**, *51*, 1127–1133. [[CrossRef](#)]
36. Yan, Y.; Wu, G.; Huang, W.; Zhang, L.; Li, L.; Yang, Z. Numerical comparison study of methane catalytic combustion characteristic between newly proposed opposed counter-flow micro-combustor and the conventional ones. *Energy* **2019**, *170*, 403–410. [[CrossRef](#)]
37. Wan, J.; Wu, Y.; Zhao, H. Excess enthalpy combustion of methane-air in a novel micro non-premixed combustor with a flame holder and preheating channels. *Fuel* **2020**, *271*, 117518. [[CrossRef](#)]
38. Zuo, W.; Jiaqiang, E.; Lin, R.; Jin, Y.; Han, D. Numerical investigations on different configurations of a four-channel meso-scale planar combustor fueled by hydrogen/air mixture. *Energy Convers. Manag.* **2018**, *160*, 1–13. [[CrossRef](#)]
39. Shih, H.-Y.; Huang, Y.-C. Thermal design and model analysis of the Swiss-roll recuperator for an innovative micro gas turbine. *Appl. Therm. Eng.* **2009**, *29*, 1493–1499. [[CrossRef](#)]
40. Wang, S.; Yuan, Z.; Fan, A. Experimental investigation on non-premixed CH₄/air combustion in a novel miniature Swiss-roll combustor. *Chem. Eng. Process.-Process Intensif.* **2019**, *139*, 44–50. [[CrossRef](#)]
41. Zhong, B.-J.; Wang, J.-H. Experimental study on premixed CH₄/air mixture combustion in micro Swiss-roll combustors. *Combust. Flame* **2010**, *157*, 2222–2229. [[CrossRef](#)]

42. Zhao, D.; Ang, L.; Ji, C.Z. Numerical and experimental investigation of the acoustic damping effect of single-layer perforated liners with joint bias-grazing flow. *J. Sound Vib.* **2015**, *342*, 152–167. [[CrossRef](#)]
43. Zhao, D. A real-time plane-wave decomposition algorithm for characterizing perforated liners damping at multiple mode frequencies. *J. Acoust. Soc. Am.* **2011**, *129*, 1184–1192. [[CrossRef](#)] [[PubMed](#)]
44. Ni, S.; Zhao, D.; Zhu, X. Heat transfer and entropy production evaluation on premixed hydrogen/air-fuelled micro-combustors with internal threads. *Fuel* **2021**, *303*, 121325. [[CrossRef](#)]
45. Yang, W.M.; Chua, K.J.; Pan, J.F.; Jiang, D.Y.; An, H. Development of micro-thermophotovoltaic power generator with heat recuperation. *Energy Convers. Manag.* **2014**, *78*, 81–87. [[CrossRef](#)]
46. Ni, S.; Zhao, D. NO_x emission reduction in ammonia-powered micro-combustors by partially inserting porous medium under fuel-rich condition. *Chem. Eng. J.* **2022**, *434*, 134680. [[CrossRef](#)]
47. Chen, X.; Li, J.; Feng, M.; Zhao, D.; Shi, B.; Wang, N. Flame stability and combustion characteristics of liquid fuel in a meso-scale burner with porous media. *Fuel* **2019**, *251*, 249–259. [[CrossRef](#)]
48. Chen, X.; Li, J.; Zhao, D.; Song, A.; Zhou, X.; Wang, N. Experimental investigation on propagation characteristics of n-heptane/air combustion wave in foamed porous media. *Fuel* **2021**, *306*, 121742. [[CrossRef](#)]
49. Chou, S.K.; Yang, W.M.; Li, J.; Li, Z.W. Porous media combustion for micro thermophotovoltaic system applications. *Appl. Energy* **2010**, *87*, 2862–2867. [[CrossRef](#)]
50. Yan, Y.; Zhang, C.; Wu, G.; Feng, S.; Yang, Z. Numerical study on methane/air combustion characteristics in a heat-recirculating micro combustor embedded with porous media. *Int. J. Hydrogen Energy* **2022**, *47*, 20999–21012. [[CrossRef](#)]
51. Yang, W.M.; Chou, S.K.; Chua, K.J.; Li, J.; Zhao, X. Research on modular micro combustor-radiator with and without porous media. *Chem. Eng. J.* **2011**, *168*, 799–802. [[CrossRef](#)]
52. Maghsoudi, P.; Gholami, J.; Gharehghani, A.; Moshari, S. Evaluation of thermo photovoltaic performance through aluminum-fueled combustor with partially porous medium and different geometric cross-sections. *Energy Convers. Manag.* **2021**, *247*, 114765. [[CrossRef](#)]
53. Bazooyar, B.; Gohari Darabkhani, H. Analysis of flame stabilization to a thermo-photovoltaic micro-combustor step in turbulent premixed hydrogen flame. *Fuel* **2019**, *257*, 115989. [[CrossRef](#)]
54. Yan, Y.; Liu, Y.; Li, L.; Cui, Y.; Zhang, L.; Yang, Z.; Zhang, Z. Numerical comparison of H₂/air catalytic combustion characteristic of micro-combustors with a conventional, slotted or controllable slotted bluff body. *Energy* **2019**, *189*, 116242. [[CrossRef](#)]
55. Yan, Y.; Yan, H.; Zhang, L.; Li, L.; Zhu, J.; Zhang, Z. Numerical investigation on combustion characteristics of methane/air in a micro-combustor with a regular triangular pyramid bluff body. *Int. J. Hydrogen Energy* **2018**, *43*, 7581–7590. [[CrossRef](#)]
56. Hosseini, S.E.; Wahid, M.A. Investigation of bluff-body micro-flameless combustion. *Energy Convers. Manag.* **2014**, *88*, 120–128. [[CrossRef](#)]
57. Niu, J.; Ran, J.; Li, L.; Du, X.; Wang, R.; Ran, M. Effects of trapezoidal bluff bodies on blow out limit of methane/air combustion in a micro-channel. *Appl. Therm. Eng.* **2016**, *95*, 454–461. [[CrossRef](#)]
58. Ji, C.; Zhao, D.; Li, X.; Li, S.; Li, J. Nonorthogonality analysis of a thermoacoustic system with a premixed V-shaped flame. *Energy Convers. Manag.* **2014**, *85*, 102–111. [[CrossRef](#)]
59. Wan, J.; Fan, A.; Yao, H.; Liu, W. A non-monotonic variation of blow-off limit of premixed CH₄/air flames in mesoscale cavity-combustors with different thermal conductivities. *Fuel* **2015**, *159*, 1–6. [[CrossRef](#)]
60. Ran, J.; Li, L.; Du, X.; Wang, R.; Pan, W.; Tang, W. Numerical investigations on characteristics of methane catalytic combustion in micro-channels with a concave or convex wall cavity. *Energy Convers. Manag.* **2015**, *97*, 188–195. [[CrossRef](#)]
61. Ni, S.; Zhao, D.; Sun, Y.; Jiaqiang, E. Numerical and entropy studies of hydrogen-fuelled micro-combustors with different geometric shaped ribs. *Int. J. Hydrogen Energy* **2019**, *44*, 7692–7705. [[CrossRef](#)]
62. Ni, S.; Zhao, D.; Becker, S.; Tang, A. Thermodynamics and entropy generation studies of a T-shaped micro-combustor: Effects of porous medium and ring-shaped ribs. *Appl. Therm. Eng.* **2020**, *175*, 115374. [[CrossRef](#)]
63. Ni, S.; Zhao, D.; You, Y.; Huang, Y.; Wang, B.; Su, Y. NO_x emission and energy conversion efficiency studies on ammonia-powered micro-combustor with ring-shaped ribs in fuel-rich combustion. *J. Clean. Prod.* **2021**, *320*, 128901. [[CrossRef](#)]
64. Xu, F.; Yan, Y.; He, Z.; Yang, Z.; Zhang, L. Numerical study on the influence of controllable flow ratio on combustion characteristics of a controllable central slotted bluff body and cavity combined micro combustor. *Int. J. Hydrogen Energy* **2021**, *46*, 6901–6914. [[CrossRef](#)]
65. Zhang, L.; Zhu, J.; Yan, Y.; Guo, H.; Yang, Z. Numerical investigation on the combustion characteristics of methane/air in a micro-combustor with a hollow hemispherical bluff body. *Energy Convers. Manag.* **2015**, *94*, 293–299. [[CrossRef](#)]
66. Yan, Y.; He, Z.; Xu, Q.; Zhang, L.; Li, L.; Yang, Z.; Ran, J. Numerical study on premixed hydrogen/air combustion characteristics in micro-combustor with slits on both sides of the bluff body. *Int. J. Hydrogen Energy* **2019**, *44*, 1998–2012. [[CrossRef](#)]
67. Zuo, H.; Zhu, Y.; Wu, S.; Abubakar, S.; Li, Y. Effect of a crossed-semicircular-plate on thermal performance of micro-combustor fueled by premixed hydrogen-air mixture. *Int. J. Hydrogen Energy* **2022**, *47*, 17442–17453. [[CrossRef](#)]
68. Malushte, M.; Kumar, S. Flame dynamics in a stepped micro-combustor for non-adiabatic wall conditions. *Therm. Sci. Eng. Prog.* **2019**, *13*, 100394. [[CrossRef](#)]
69. Chen, L.; Asai, K.; Nonomura, T.; Xi, G.; Liu, T. A review of Backward-Facing Step (BFS) flow mechanisms, heat transfer and control. *Therm. Sci. Eng. Prog.* **2018**, *6*, 194–216. [[CrossRef](#)]

70. Tan, Y.; Jiaqiang, E.; Chen, J.; Liao, G.; Zhang, F.; Li, J. Investigation on combustion characteristics and thermal performance of a three rearward-step structure micro combustor fueled by premixed hydrogen/air. *Renew. Energy* **2022**, *186*, 486–504. [[CrossRef](#)]
71. Peng, Q.; Jiaqiang, E.; Zhang, Z.; Hu, W.; Zhao, X. Investigation on the effects of front-cavity on flame location and thermal performance of a cylindrical micro combustor. *Appl. Therm. Eng.* **2018**, *130*, 541–551. [[CrossRef](#)]
72. Zuo, W.; Zhang, Y.; Li, Q.; Li, J.; He, Z. Numerical investigations on hydrogen-fueled micro-cylindrical combustors with cavity for micro-thermophotovoltaic applications. *Energy* **2021**, *223*, 120098. [[CrossRef](#)]
73. Su, Y.; Song, J.; Chai, J.; Cheng, Q.; Luo, Z.; Lou, C.; Fu, P. Numerical investigation of a novel micro combustor with double-cavity for micro-thermophotovoltaic system. *Energy Convers. Manag.* **2015**, *106*, 173–180. [[CrossRef](#)]
74. Cai, T.; Zhao, D.; Karimi, N. Optimizing thermal performance and exergy efficiency in hydrogen-fueled meso-combustors by applying a bluff-body. *J. Clean. Prod.* **2021**, *311*, 127573. [[CrossRef](#)]
75. Cai, T.; Sun, Y.; Zhao, D. Enhancing heat transfer performance analyses of a hydrogen-fueled meso-combustor with staggered bluff-bodies. *Fuel Process. Technol.* **2021**, *218*, 106867. [[CrossRef](#)]
76. Zuo, W.; Jiaqiang, E.; Liu, H.; Peng, Q.; Zhao, X.; Zhang, Z. Numerical investigations on an improved micro-cylindrical combustor with rectangular rib for enhancing heat transfer. *Appl. Energy* **2016**, *184*, 77–87. [[CrossRef](#)]
77. Akhtar, S.; Khan, M.N.; Kurnia, J.C.; Shamim, T. Investigation of energy conversion and flame stability in a curved micro-combustor for thermo-photovoltaic (TPV) applications. *Appl. Energy* **2017**, *192*, 134–145. [[CrossRef](#)]
78. Wan, J.; Zhao, H. Laminar non-premixed flame patterns in compact micro disc-combustor with annular step and radial preheated channel. *Combust. Flame* **2021**, *227*, 465–480. [[CrossRef](#)]
79. Mansouri, Z. Combustion in wavy micro-channels for thermo-photovoltaic applications—Part I: Effects of wavy wall geometry, wall temperature profile and reaction mechanism. *Energy Convers. Manag.* **2019**, *198*, 111155. [[CrossRef](#)]
80. Yang, X.; He, Z.; Cha, S.; Zhao, L.; Dong, S.; Tan, H. Parametric analysis on the combustion and thermal performance of a swirl micro-combustor for micro thermophotovoltaic system. *Energy* **2020**, *198*, 117312. [[CrossRef](#)]
81. Zhao, H.; Zhao, D.; Becker, S. Entropy production and enhanced thermal performance studies on counter-flow double-channel hydrogen/ammonia-fuelled micro-combustors with different shaped internal threads. *Int. J. Hydrogen Energy* **2022**, *47*, 36306–36322. [[CrossRef](#)]
82. Zhao, H.; Li, G.; Zhao, D.; Zhang, Z.; Sun, D.; Yang, W.; Li, S.; Lu, Z.; Zheng, Y. Experimental study of equivalence ratio and fuel flow rate effects on nonlinear thermoacoustic instability in a swirl combustor. *Appl. Energy* **2017**, *208*, 123–131. [[CrossRef](#)]
83. Jiang, N.; Studer, E.; Podvin, B. Physical modeling of simultaneous heat and mass transfer: Species interdiffusion, Soret effect and Dufour effect. *Int. J. Heat Mass Transf.* **2020**, *156*, 119758. [[CrossRef](#)]
84. Smoke, M.D.; Giovangigli, V. Formulation of the premixed and nonpremixed test problems. In *Reduced Kinetic Mechanisms and Asymptotic Approximations for Methane-Air Flames*; Springer: Berlin/Heidelberg, Germany, 1991; pp. 1–28.
85. Li, J.; Chou, S.K.; Yang, W.M.; Li, Z.W. A numerical study on premixed micro-combustion of CH₄-air mixture: Effects of combustor size, geometry and boundary conditions on flame temperature. *Chem. Eng. J.* **2009**, *150*, 213–222. [[CrossRef](#)]
86. Cai, T.; Tang, A.; Zhao, D.; Zhou, C.; Huang, Q. Flame dynamics and stability of premixed methane/air in micro-planar quartz combustors. *Energy* **2020**, *193*, 116767. [[CrossRef](#)]

Disclaimer/Publisher's Note: The statements, opinions and data contained in all publications are solely those of the individual author(s) and contributor(s) and not of MDPI and/or the editor(s). MDPI and/or the editor(s) disclaim responsibility for any injury to people or property resulting from any ideas, methods, instructions or products referred to in the content.